Design and Analysis
of a Novel Omnidirectional Step-climbing Robot

Jian Wei,[1,2] Chi-Hsin Yang,[1*] Shouqiang Chen,[3]
Hao Gao,[1] and Kun-Chieh Wang[1]

[1]School of Mechanical and Electric Engineering, Sanming University, Sanming 365004, Fujian Province, China
[2]Fujian University Engineering Research Center of Modern Mechanical Design and Manufacturing Technology,
Sanming 365004, Fujian Province, China
[3]Sanming Steel (Group) Kinetic Energy Co., Ltd., Sanming 365000, Fujian Province, China

We propose a novel omnidirectional step-climbing robot capable of moving in all directions on the ground and climbing steps. To achieve this, we present the construction and design of a robot equipped with four innovative equilateral triangle-type chain wheels (ETCWs) and two elevation-adjusting modules (EAMs). The designed ETCWs, which are arranged around multiple roller assemblies, facilitate step-climbing by creating small gaps between roller assemblies when the wheel comes in contact with the uneven ground. The corners of steps become stuck in the small gaps of ETCWs, preventing slipping during step-climbing. The designed EAM is used to adjust the height of the robot's base frame adaptively to avoid terrain obstacles, referring to signals from front ultrasonic sensors. Static analysis models for the main support frames are developed, and a case study on motion trajectory planning is also conducted.

1. Introduction

In the field of human production activities, mobile robots (MRs) have become essential equipment. The integration of MRs expands the scope of collaboration between humans and machines, further increasing the efficiency and accuracy of work tasks. Various types of MR, including legged, tracked, wheeled, and hybrid locomotion robots, have been developed for numerous practical applications.[1] Wheeled mobile robots (WMRs) are particularly well studied and commonly applied owing to their simple structure, ease of control, and ability to move at high speeds on flat surfaces. As a result, they have attracted significant attention in applications such as environmental monitoring,[2–4] logistics operations,[5–7] warehouse management,[8–10] agricultural practices,[11–13] and construction projects.[14–16] However, WMRs face challenges when navigating complex terrains such as rough roads and steps. Ongoing research is focused on improving the maneuverability of WMRs in order to overcome these obstacles. Recently,

---

developed solutions have involved combining two forms of locomotion, wheeled and legged, to address this issue. [17–20]

Legged robots are designed to overcome terrain obstacles and execute movements smoothly, but their main drawback is the low speed of movement.[21–23] Additionally, in unfamiliar terrain, the balancing control problem during dynamic stepping is complex.[24–26] Recent research has focused on improving the motion speed of legged robots.[27,28] MRs with multiwheel or track structures have been found to be effective for assisting robots in climbing steps.[29–32] Baishya *et al.* collated and analyzed various existing types of step-climbing robot, such as the leggy type, track type, hybrid leggy–track type, and two-wheel and three-wheel cluster types, and provided a qualitative comparison of their advantages and disadvantages.[32]

The four-wheeled robot equipped with Mecanum wheels,[33–35] driven by four independent servomotors, is capable of moving in any direction on a plane without requiring the prior rotational adjustment of the robot body.[36,37] This mechanism is widely utilized in industrial applications for WMRs.[7,13,38] To achieve omnidirectional movement and step-climbing capabilities simultaneously, there is a significant research focus on developing new robot architectures based on the Mecanum wheel structure. One main drawback of using Mecanum wheels for step-climbing is the limited contact area between the wheel and the step surface, resulting in insufficient support and friction, leading to slippage. However, various solutions have been proposed in the existing literature to address these shortcomings.[1,39–42]

In Ref. 39, the spiral Mecanum wheel, consisting of spiral beams with arranged small rollers, was introduced for achieving step-climbing capabilities in robots. In Ref. 40, a hexapod robot was proposed to traverse steps using three-link mechanical legs with Mecanum wheels at the ends. In Ref. 1, a new spoked Mecanum wheel composed of four links with fixed rollers at the ends was designed to enable the robot to move across various terrains. Baishya *et al.* addressed an antislip mechanism for the Mecanum wheel of a step-climbing robot using shape memory alloy actuation.[41] Finally, an MR mounted on multi-omnidirectional tracks, similar in structure to traditional Mecanum wheels with surrounding rollers, was developed for omnidirectional movement and step-climbing.[42]

Motivated by the aforementioned works, a novel omnidirectional step-climbing robot is presented, which is capable of moving in all directions on the ground and traversing steps. The contributions of this study are outlined below.

(1) To achieve smooth climbing and omnidirectional movement, the proposed robot is composed of four innovatively designed equilateral triangle-type chain wheels (ETCWs) driven by servomotors. The novel ETCW consists primarily of an equilaterally triangular support frame and multiple arranged roller assemblies. The virtual line track is formed by the roller assemblies on one side of the ETCW.

(2) To enhance the nonslip effect during robot step-climbing, a ring spring is incorporated into each roller assembly to absorb movement vibrations. Additionally, a small gap is automatically created between two roller assemblies when the ETCW encounters uneven ground. During step-climbing, when the ETCW makes contact with the corner point of a step, the corner point becomes wedged in the small gap between the roller assemblies.

(3) To prevent collision between the robot's base frame and the ground, an elevation-adjusting module (EAM) actuated by two remote control (RC) servomotors is utilized. The robot is capable of adapting to uneven terrain during movement by dynamically adjusting the elevations of its four corners using the designed EAM. Additionally, when the climbing process begins, the front ultrasonic sensors detect steps and estimate their heights, allowing for the appropriate adjustment of the robot's bottom by the module.

The rest of the paper is outlined as follows. In Sect. 2, we introduce the arrangement of the novel omnidirectional step-climbing and describe the principles of movement. The detailed designs of the ETCW, EAM, and other supported parts of the robot are clearly described in Sect. 3. The structure design of the 3D mechanism model and static analysis for all components are conducted using SOLIDWORKS and MATLAB/SIMULINK tools. In Sect. 4, the inverse kinematics of the robot are discussed, and a case study on motion trajectory planning is carried out. The overall assembly of the omnidirectional step-climbing robot is summarized in Sect. 5, with conclusions given in Sect. 6.

2.   Omnidirectional Step-climbing Robot

2.1   Arrangement of robot

The designed model of the omnidirectional step-climbing robot is shown in Fig. 1. Figure 1(a) shows that four wheels are driven by servomotors (1) to (4) and two EAMs (5) and (6), which are
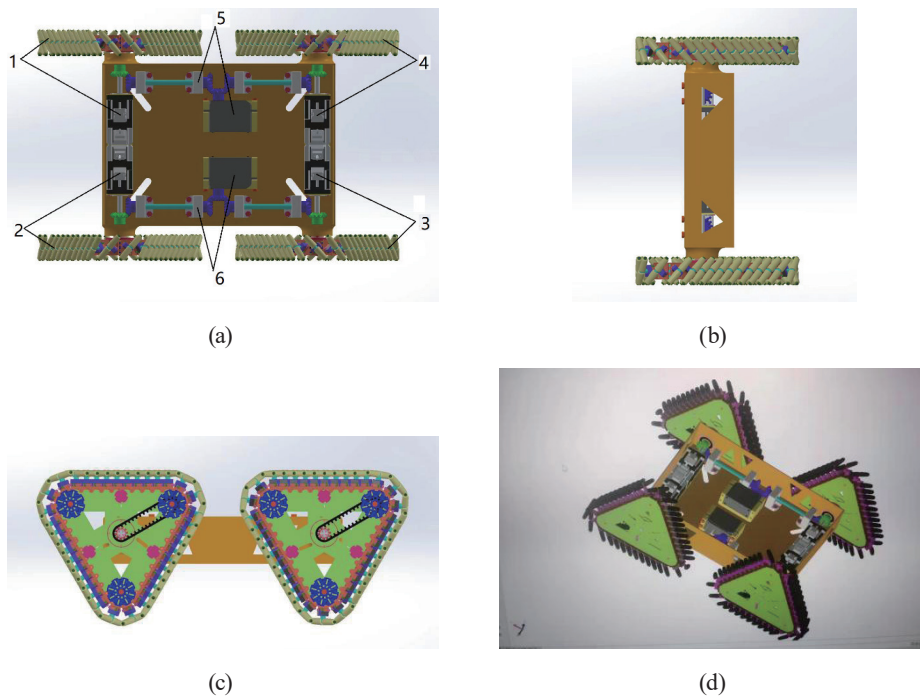

Fig. 1.   (Color online) Designed omnidirectional step-climbing robot. (a) Top, (b) front, and (c) left-side views, and (d) isometric projection.

actuated by RC servomotors, are mounted on the base frame of the robot. Before the robot performs step-climbing, in order to avoid the collision of the base frame with the step, it is necessary to raise the base frame by utilizing the EAMs (5) and (6). In Fig. 1(c), the ETCWs on the left side of the robot are shown. The robot with the ETCWs can omnidirectionally move on the ground and pass over the step. The analysis and design of the structure of an ETCW are described later. Figure 1(d) shows the view of isometric projection.

2.2 Motion planning of robot

Robot motion planning is mainly divided into two categories, namely, the movement in the plane and the step-climbing. The robot moves in all directions on a plane by individually and suitably controlling the spinning directions and speeds of the four ETCWs. As shown in Fig. 2, the robot carries out the forward/backward and rightward/leftward translational movements, in which the red arrow at the edge of the wheel represents the moving direction of each wheel, while the blue arrow represents the moving direction of the robot. The moving direction and speed of the robot are determined by tuning the rotational direction and spinning speed of each ETCW.

The climbing process of the robot is shown in Fig. 3. Figure 3(a) shows that the robot moves forward and the front ultrasonic sensors of the robot detect the step, and the height of the step is estimated. Then, the step-climbing mode is activated on. According to the estimated step height, the height of the bottom of the robot is suitably raised by the EAMs. Then, the ETCWs in front of the robot come in contact with the corner of the step, as shown in Fig. 3(b). In Figs. 3(c) and 3(d), the corner of the step is stuck in a small gap between two roller assemblies around the ETCW to provide the robot climbing force and complete the step-climbing of the robot without slipping.

3. Designed Modules of Robot

In this study, to achieve the omnidirectional movement and step-climbing of the robot, the detailed designs of the ETCW, EAM, and other supported parts are introduced as follows.
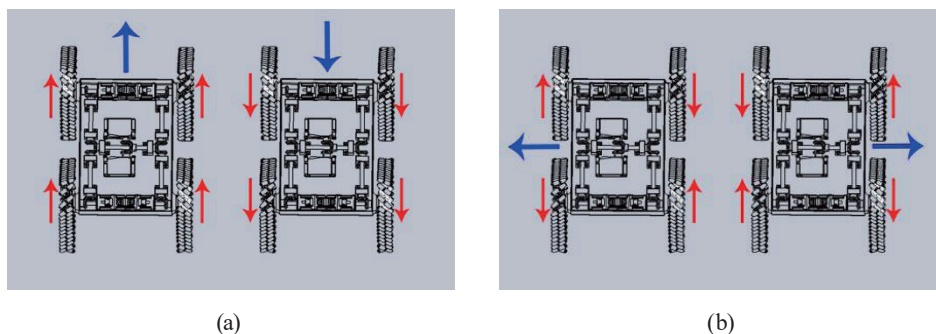

| (a) | (b) |

Fig. 2.   (Color online) Direction of movement of robot. (a) Forward/backward and (b) moves left/right.
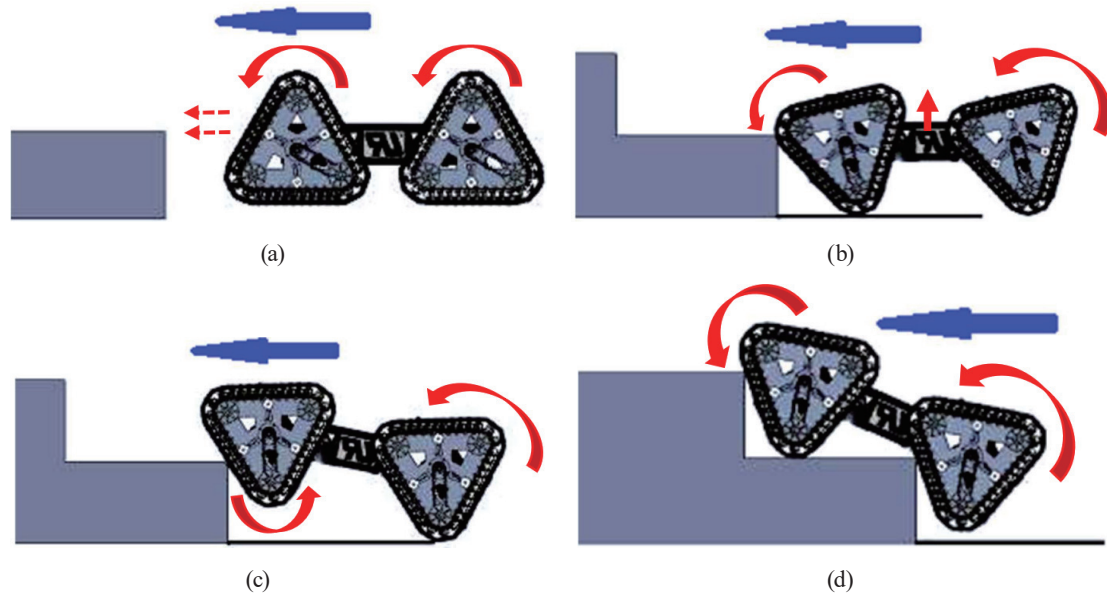
Fig. 3.   (Color online) Working principle of step-climbing of robot. (a) Forward movement, (b) tuning the height, (c) front ETCWs climbing a step, and (d) robot climbing steps.

3.1   Design of ETCW

To achieve movement and smooth step-climbing, the novel ETCW is designed. The designed structure of the wheel is shown in Fig. 4. The novel ETCW consists of the equilaterally triangular support frame (1), the tensional wheel (2), the belt wheel (3), the conveyer belt (4), the sprocket (5), and the rolling chain (6). Multiple roller assemblies (8) are connected with the rolling chain to form the virtual track (7) around the triangular wheel. The belt wheel (3) is connected to a servomotor to provide the mobile power of the ETCW. The spined sprocket (5) is driven by the belt wheel (3) through the conveyor belt (4). The rolling chain (6), which occupies the roller assemblies (8), is driven by the spined sprocket (5). Furthermore, the virtual track (7), which is formed by the envelope of roller assemblies (8) and tensioned by the tensional wheel (2), is run around the wheel to realize the movement.

3.1.1   Design of roller assembly

The design concept of the ETCW in Fig. 4 is similar to that of the Mecanum wheel,[33–35] which is arranged by the rollers around the wheel. The structure of the roller assembly (8) in Fig. 4 is shown in Fig. 5. The roller assembly consists of the roller (1), the spindle (2), the middle support (3), the chain link buckle (4), the ring spring (5), and the chain link (6). To ensure smooth robot movement, the ring spring (5) provides the damping effect to avoid the vibration of the robot during movement.
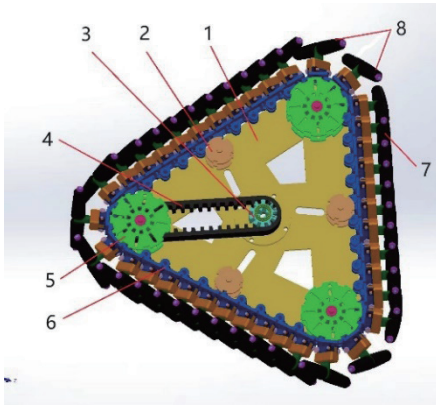
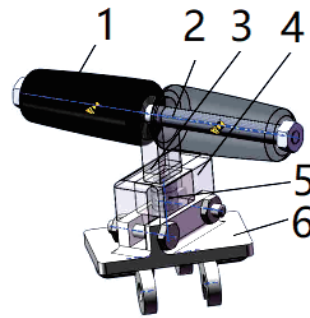Fig. 4. (Color online) Equilateral triangle-type chain wheel.

Fig. 5. (Color online) Structure of roller assembly.

3.1.2 Shape design of a roller

The rollers on the end of the roller assembly, which are positioned around the ETCW and make contact with the ground while in motion, rotate on the spindle (2) in addition to moving around the wheel's central axis, because of the friction created between the ground and the roller. The velocity vector generated by the revolution and rotation of the roller realizes the omnidirectional movement of the robot. For the Mecanum wheel,[33] to ensure the smoothness of the overall rolling motion of the wheel, the envelope formed by the rollers around the Mecanum wheel is designed to be close to a circle. The entire triangular wheel body type for the ETCW is encircled by rollers. One side of the ETCW is in contact with the ground during the movement. The enclosed rollers' envelope creates the virtual contacting track, which is intended to be a flat line. For this reason, the shape of the roller must be designed to obtain a linear track on one side of the ETCW.

The design cylinder [33] seen in Fig. 6 serves as the basis for the shape design of the roller. The red curve from A to C and B is the shape to be designed for a roller.

In Fig. 6, the center O of the bottom circle of the cylinder is taken as the origin of the coordinate system. The upward direction of the cylinder axis is taken as the positive direction of the *z*-axis, and an *O-xyz* space-rectangular coordinate system is established by using the right-hand rule. By selecting point B on the upper circle and point A on the bottom circle of the cylinder, the line segment $\overline{AB}$ connecting two points A and B becomes the spindle-axis length of the roller. The arc $\overgroup{AB}$ along the outer surface of the cylinder is the shape of the roller.

The vertical line segment $\overline{BF}$ from point B to the bottom circle intersects the bottom circle at point F. The contact point C between the roller and the ground is chosen on the arc $\overgroup{AB}$. The perpendicular line from point C to the spindle-axis $\overline{AB}$ intersects $\overline{AB}$ at point K. The vertical line $\overline{KM}$ from point K to the bottom circle intersects $\overline{AF}$ at point M.

In the coordinate system *O-xyz*, if the coordinates of origin O are (0, 0, 0), then the coordinates of point B are ($R\cos\gamma$, $R\sin\gamma$, H) and the coordinates of point A are (R, 0, 0), where R and H are the theoretical radius and width of the roller, respectively. γ is the central angle of the
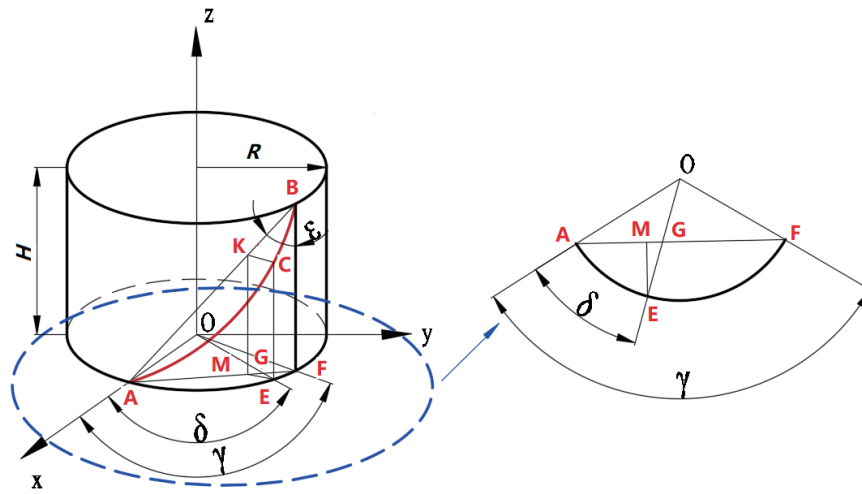
Fig. 6.   (Color online) Design cylinder for shape of roller.

roller shape projected on the bottom circle. In the right triangle $\triangle ABF$, $\overline{AF} = \overline{BF} = H$. In the isosceles triangle $\triangle AOF$, $\overline{AF} = 2R\sin(\gamma/2)$. γ is defined by

$$\gamma = 2\arcsin\frac{\overline{AF}}{2R} = 2\arcsin\frac{H}{2R}. \tag{1}$$

On the plane normal to the axis line $\overline{AB}$, the shape of the roller is formed by a point in the circle with radius r of

$$r = \overline{CK} = \overline{EM} = \overline{AE}\sin\left(\frac{\gamma - \delta}{2}\right) = 2R\sin\frac{\delta}{2}\sin\left(\frac{\gamma - \delta}{2}\right), \tag{2}$$

where δ is the central angle formed by the projection of the contact point between the roller and the ground on the bottom circle, and $0 \le \delta \le \gamma$. When $\delta = \gamma/2$, the radius of the roller is maximum, $r = r_{max}$, and when $\delta = \gamma$, the radius of the roller is minimum, $r = r_{min}$.

The axis length l is evaluated as

$$l = \overline{AK} = \frac{\overline{AM}}{\sin\varepsilon} = \sqrt{2} \cdot \overline{AM} = \sqrt{2} \cdot \overline{AE} \cdot \cos\left(\frac{\gamma - \delta}{2}\right)$$
$$= 2\sqrt{2}R\sin\frac{\delta}{2}\cos\left(\frac{\gamma - \delta}{2}\right), \tag{3}$$

where ε is the angle between the axis of the roller and the axis of the cylinder with $\varepsilon = 45°$. By combining Eqs. (2) and (3), the variables r, l form an ellipse, and the equation is obtained as

$$r^2 + \frac{l^2}{2} = 4R^2 \sin^2\left(\frac{\delta}{2}\right).$$

(4)

By setting $R = 50$ mm, the shapes of rollers with three different H values are as shown in Fig. 7. In the case of $(R, H) = (50, 45)$, $\gamma = 53.486°$ is obtained from Eq. (1). For the spindle at the length interval $l \in [15.559, 48.888]$ mm, the maximum and minimum radii of the rollers are $r_{max} = 5.42$ mm and $r_{min} = 4.047$ mm. The final designed model of the rollers with the spindle is shown in Fig. 8.

3.1.3 Placement of rollers around ETCW

The Mecanum wheel,[33] which takes up the rollers around the wheel and has omnidirectional movement capabilities, and the ETCW share a similar design concept. As illustrated in Fig. 9, there are two different ways that rollers are placed around a wheel, namely, the two-ends-supported and middle-supported varieties.
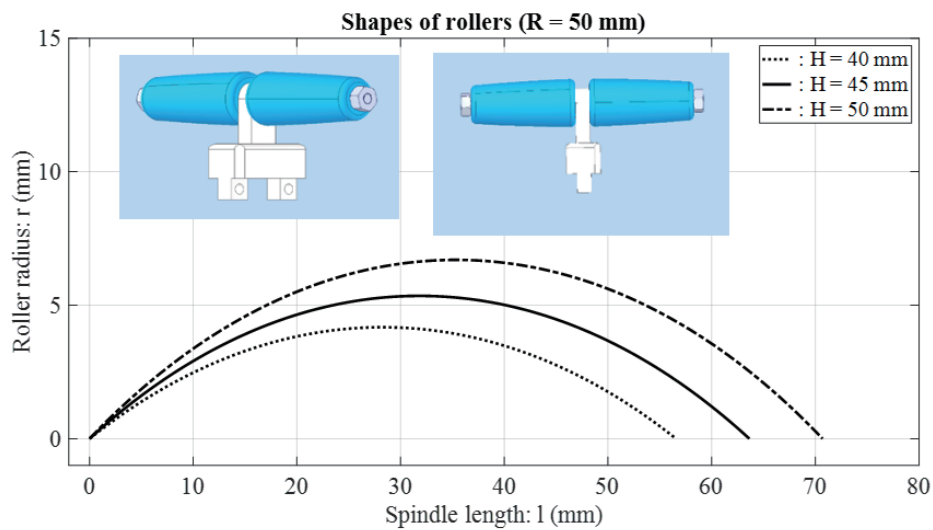

Fig. 7.   (Color online) Shapes of rollers with different H values.

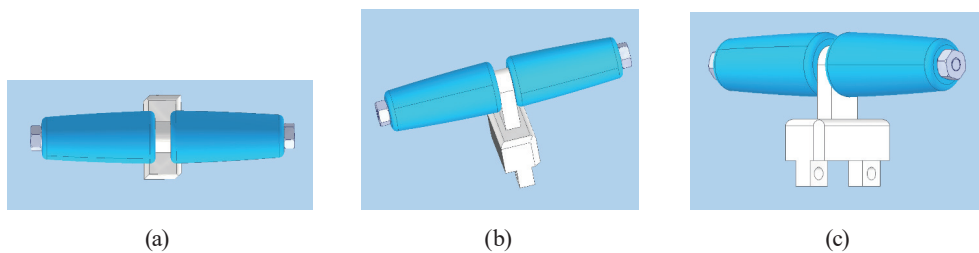(a)   (b)   (c)

Fig. 8.   (Color online) Designed model of the rollers with spindle for $(R, H) = (50, 45)$ mm. (a) Top, (b) front, and (c) squint-angle views.

Fig. 9.   (Color online) Placement types of rollers around wheel. (a) Two-ends-supported and (b) middle-supported types.

In the two-ends-supported type of placement, the wheel contains two circular supported plates, and the spindles of all the rollers are mounted on the plates, as shown in Fig. 9(a). When the robot moves, the working forces are mainly carried by the spindles and circular supported plates. The wheel with two-ends-supported rollers is not suitable for step-climbing because no effected forces are generated for climbing steps. Slip occurs between the corner of the step and the wheel.

In the middle-supported type of placement, the roller is divided into two small rollers by the corresponding supported plate, where the spindle of small rollers is installed on it, as shown in Fig. 9(b). Two small rollers with a spindle installed on the middle-supported plate form a roller assembly. When the robot moves, the working forces are mainly undertaken by the middle section of the spindle of the roller and the supported plate. This type of roller arrangement is suitable for forming a flat virtual track of the wheel. Moreover, a small gap between the two roller assemblies is easy to produce by adding an appropriately flexible device. It provides more ability for the robot to move adaptively in different terrains. In this study, the middle-supported type of placement of rollers is applied to the proposed ETCW.

3.1.4   Design of ring spring

When the robot performs step-climbing, a slip between the ETCW and the corner of the step occurs. To overcome this drawback, a ring spring is installed in the roller assembly, as shown in Fig. 5. This ring spring is an important device for absorbing the vibration of the robot during step-climbing. A tiny space is also created between two roller assemblies when the ETCW contacts uneven terrain owing to the ring spring's addition to the roller assembly. A nonslip effect is produced for the wheel during step-climbing when the ETCW makes contact with the step's corner point and is trapped in the small space between roller assemblies.

The specifications of the ring spring are satisfied by considering the maximum axial load of the roller assemblies in the four ETCWs, putting the robot's weight at 6 kg, and allowing a gap of 4 mm between two roller assemblies. By utilizing the developed spring design system,[43] the deformation, the outer-ring diameter, and the height of the ring spring are chosen as 4.19, 4, and 9.9 mm, respectively. Moreover, the cone surface and friction angles of the ring spring are evaluated as 4.1° and 2.05°, respectively.[44]

3.1.5 Number of occupied roller assemblies

The ETCW is driven by the servomotor with suitable output torque and power. Considering the case of step-climbing depicted in Fig. 3(d), it is assumed that the robot weighs 6 kgw and climbs a step with a width of 300 mm and a height of 150 mm. The mechanical model shown in Fig. 10 is established.

Considering the model shown in Fig. 10 with force balance, the force equations are obtained as

$$f_1 \cos\eta + f_2 = f_{N1} \sin\eta, \tag{5}$$

$$G = f_1 \sin\eta + f_{N1} \cos\eta + f_{N2}, \tag{6}$$

$$\tau_w = \tau + f_{N2}L\cos(\eta + 30°) - f_1 L \sin 30° \\ - f_{N1}(150\csc\eta - L\cos 30°) - f_2 L \sin(\eta + 30°), \tag{7}$$

where f_{N1}, f_{N2} are the supporting forces of the robot, G is the total force acting on the step for a wheel, and τ_w is the required moment for step-climbing motion. $f_1 = \mu f_{N1}$ and $f_2 = \mu f_{N2}$ are friction forces with the friction coefficient μ. τ is the driving torque provided by a servomotor. L is the length of the rotational center to the triangular point of the ETCW and η is the angle between the track of the ETCW and the step.

In Fig. 3(a), the servomotors provide power to drive the ETCWs for movement before step-climbing. When the robot climbs the step, as shown in Fig. 3(c), only the front ETCWs make contact with the corner of the step. In this case, both f_{N2} and f_2 are zero and the servomotors need more torque to overcome f_{N1} and f_1. In Fig. 3(d), when the robot raises the rear ETCWs, the stress point of f_{N1} is 180 mm away from the side of the step, where the angle η is minimum in this case.

In the case of the movement shown in Fig. 3(a), the ETCW has the most rollers in contact with the ground. In Fig. 11, the wheel starts to be driven by the servomotor, and the starting torque T provided for the wheel is

$$T = GL\sec\psi, \tag{8}$$

where G is the weight of the ETCW and ψ is the angle between G and the tangent force $F = G\sec\psi$. When $\psi = 30°$, the rolling friction of the whole wheel is ignored and the torque T is maximum.

Considering that the total weight of the robot is small and the desired output torque of the ETCW is sufficient, the weight of a single ETCW is selected as 1.5 kgw with $L = 13.5$ mm. According to Eq. (8), the starting torque of a single ETCW is estimated to be about 0.233 Nm. Then, the total starting torque provided by the four ETCWs is 0.932 Nm. For the previously evaluated size of the roller assembly, the chain numbered 12A with pitch equaling 19.05 mm is selected.[44] The maximum length of this chain is 27.70 mm. For this length of the chain, 37
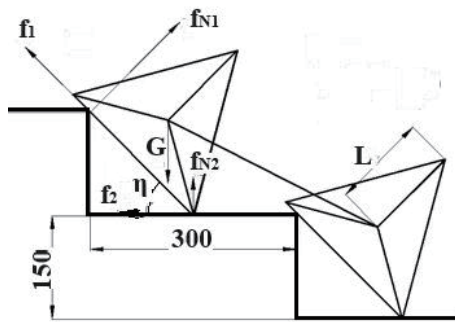
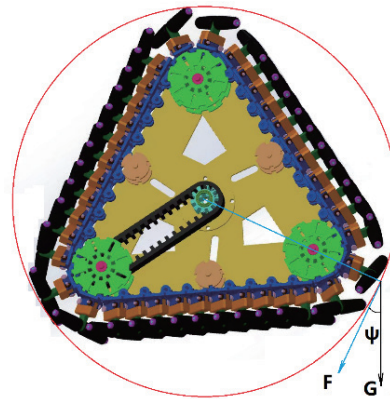Fig. 10.   Mechanical model for step-climbing.

Fig. 11.   (Color online) Starting torque of ETCW.

roller assemblies can be installed. However, the chain should have a suitable initial sag after installing the roller assemblies and the rollers on the chain should not be loose. It is finally determined that the ETCW should be installed with 38 roller assemblies.

3.1.6   Static analysis of chain link

The chain link (6) shown in Fig. 5 is an important module in the movement of the robot. When the robot moves, it is subject to the tension force from the chain and the thrust from the servomotor driving the sprocket (5) shown in Fig. 4. Moreover, the individual chain link is also subject to the gravity of the robot. The working state subject to continuous forces makes the chain link a fatigue-prone part of the robot.

Considering the required wear resistance of an ETCW, acrylonitrile butadiene styrene (ABS) material is applied. Then, the static analysis of the chain link is performed and the results are shown in Fig. 12. It is shown in Fig. 12(a) that the maximum and minimum stresses of the chain link are 45.36 and 0128 Mpa, respectively. The maximum actual applied stress is 3.78 Mpa. The actual applied stress is within the calculated safety range and there is no stress concentration. Figure 12(b) shows that the maximum and minimum deformations of the chain link are 0.015 and 0.00064 mm, respectively. Small and acceptable deformations are observed.

3.2   Design of EAM

When the robot undertakes step-climbing, the height of the base frame of the robot must be tuned to avoid collision between the base frame and the uneven ground or step. Then, the EAM for robot step-climbing is designed. As shown in Fig. 13, the second stage of bevel gears (6), the first stage of bevel gears (8), two RC servomotors (4), two fixed frames for the RC servomotor (5), the driven shafts (1), and the L-type bearing seats (2) and (3) make up the planned module. They are all fixed on the robot's base frame, along with four servomotors (7). Figure 14 shows an ETCW that is linked to the base frame via the flange (10) and the shaft with a deep-groove ball bearing (9).
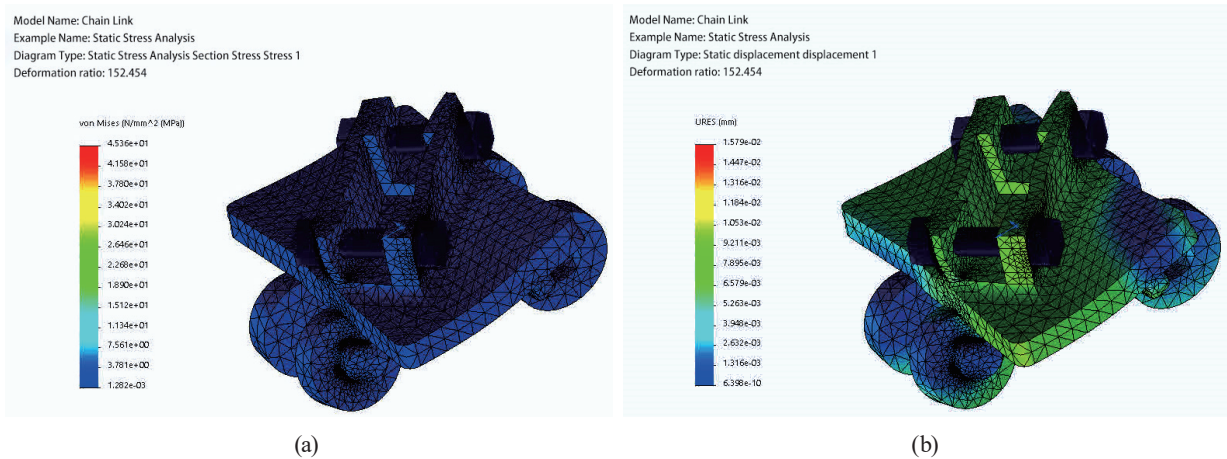
(a)

(b)

Fig. 12. (Color online) Results of static force analysis for chain link. (a) Stresses and (b) displacements.
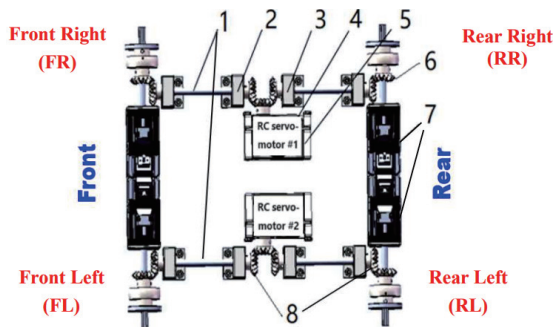

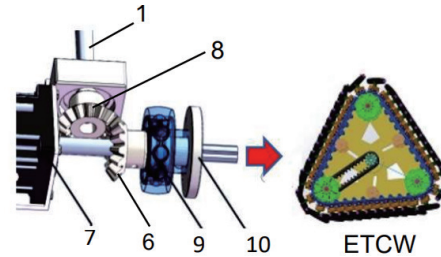Fig. 13. (Color online) Construction of EAM.

Fig. 14. (Color online) Connection between ETCW and robot.

The assembled device is mounted on the ETCW's central axis in Fig. 14. It is composed of the flange (10), the deep-groove ball bearing (9), and the second stage of bevel gears (6). The assembled device's spin remains unaffected when the servomotor (7) generates the output torque required to operate the ETCW directly. Since the RC servomotors drive the shaft (1) with the first stage of bevel gears (8), which is engaged with the second stage of bevel gears (6), the servomotors for driving the ETCWs and the RC servomotors are operated independently.

An RC servomotor is an actuator that can precisely control the clockwise (CW) and counterclockwise (CCW) rotational angles of the output shaft. When two RC servomotors individually rotate CW or CCW in the EAM, the heights of the four corners of the base frame of the robot are tuned. Figure 13 shows that the robot's front right (FR) corner descends and its rear right (RR) corner rises when RC servomotor #1 turns in a CW manner. The rear left (RL) corner rises and the front left (FL) corner falls in a similar manner when RC servomotor #2 turns in a CCW direction. The corner tuning states of the robot with two RC servomotors turning in both the CW and CCW directions are listed in Table 1.

When the CW or CCW angles of two RC servomotors in the EAMs are controlled in a suitable sequence, the robot has the ability to avoid collision with the uneven ground or step during movement or step-climbing.

Table 1
Tuning states of corners for robot by EAM.

	RC servomotor #1		RC servomotor #2	
	CCW	CW	CCW	CW
Front right (FR)	UP	DOWN	(no work)	(no work)
Front left (FL)	(no work)	(no work)	DOWN	UP
Rear right (RR)	DOWN	UP	(no work)	(no work)
Rear left (RL)	(no work)	(no work)	UP	DOWN

3.3   Finite element analysis of main supporting parts

In addition to the design and analysis for the aforementioned ETCW and EAM, the static analyses of the four main supporting parts of the robot, that is, the L-type bearing seat, the base frame of the robot, the fixed frame of the RC servomotor, and the equilaterally triangular frame of the ETCW, are required. The models are designed for carrying out the finite element analysis and the results are shown in Fig. 15. The following summary can be derived.

(1) Primarily designed to endure the torque and gravity imposed by the gearbox, the L-type bearing seat holds the driven shaft and bevel gears. We have decided to use aluminum alloy for the framework. There is no maximum resultant stress of 6.4 Mpa, as shown in Fig. 15(a). The aluminum alloy's yield limit is within reach at 320 Mpa, and the planned model is adequate.

(2) For mounting the RC servomotor on the robot's base frame, a fixed frame is utilized. The ABS material for static analysis is selected, as shown in Fig. 15(b). This illustrates the 3.8 Mpa maximal stress and the 2.219 Mpa needed stress. This condition is met by the designed model.

(3) Carbon fiber sheet T300 is used as the robot's basic frame, supporting the EAMs and torque of RC servomotors as well as servomotors used to drive ETCWs. The practical criteria are satisfied, as shown by Fig. 15(c), where the maximum stress is 0.63 Mpa and the actual needed stress is 0.36 Mpa.

(4) The full ETCW is supported by the equilaterally triangular framework. The maximum stress is 1.2 Mpa and the yield limit is 25 Mpa, which satisfies the necessary usage, as shown in Fig. 15(d).

4.   Motion Trajectory Planning of Robot

### 4.1   Inverse kinematics of ETCW

In Sect. 3, it was mentioned that the middle-supported type of roller placement is applied to form the ETCW in this study. When the robot moves, a group of rollers, which are mounted on one side of the ETCW, are in contact with the ground. The kinematics for the ETCW regarded as one roller should be analyzed. The relative motion between the roller's center and the mass center of the robot is depicted in Fig. 16. The kinematical model of a roller is also shown in Fig. 17.

Model name: L-shaped bearing seat assembly [BLC-628-2Z-25-B-MTP]
Example Name: Static Stress Analysis 1 [- BLC-628-2Z-25-B-MTP -]
Diagram type: Static stress analysis section Stress stress 1
Deformation ratio: 2.18585e+09
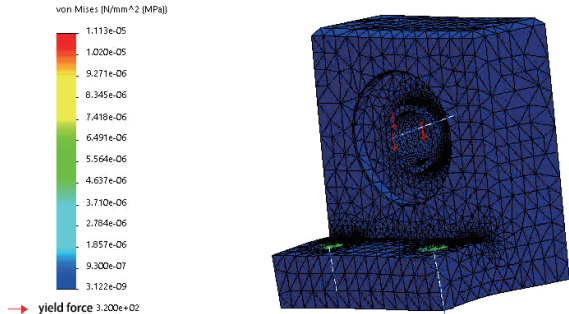
Model name: Steering gear frame
Example Name: Static stress analysis
Diagram type: Static stress analysis section Stress stress 1
Deformation ratio: 50.9288
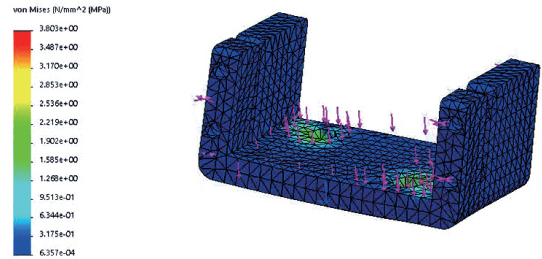
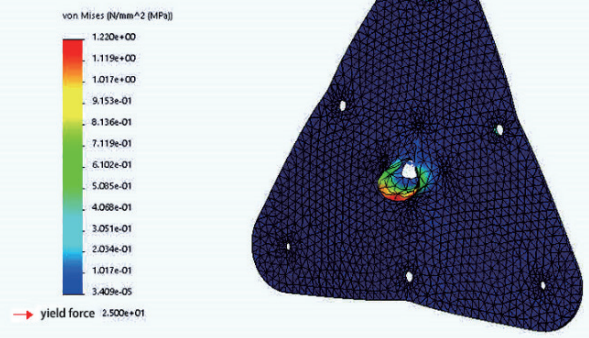(a)   (b)

Model name: lower body shell
Example Name: Static stress analysis
Diagram type: Static stress analysis section Stress stress 1
Deformation ratio: 13.3638

Model name: Triangle fixed bracket
Example Name: Static stress analysis
Diagram type: Static stress analysis section Stress stress 1
Deformation ratio: 200,000

(c)   (d)

Fig. 15.   (Color online) Finite element analysis of four supporting parts. (a) L-type bearing seat, (b) fixed frame of RC servomotor, (c) base frame of robot, and (d) equilaterally triangular frame of ETCW.
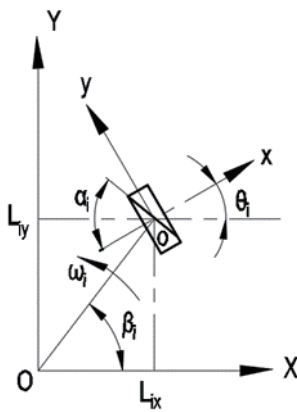
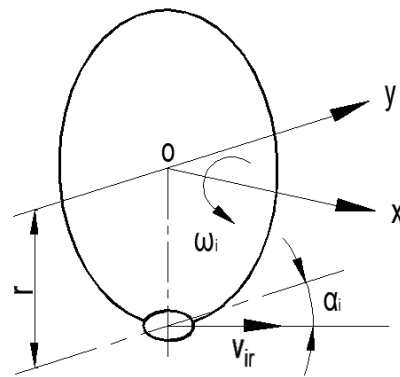Fig. 16.   Relative motion of roller and robot.   Fig. 17.   Kinematical model of roller.

According to Figs. 16 and 17, the relative velocity of the roller's center, *o*, in the local frame with coordinates *o-xy* is

$$\begin{bmatrix} v'_{ix} \\ v'_{iy} \end{bmatrix} = \begin{bmatrix} 0 & \sin\alpha_i \\ r & \cos\alpha_i \end{bmatrix}\begin{bmatrix} \omega_i \\ v_{ir} \end{bmatrix} = R_1\begin{bmatrix} \omega_i \\ v_{ir} \end{bmatrix}, \quad i = 1,2,3,4, \tag{9}$$

where v'_{ix} and v'_{iy} are the velocities in the *x*- and *y*-directions of the local frame located on the roller's center with coordinates *o-xy*, respectively. α_i is the angle of the axis normal to the roller's spindle in the local frame *o-xy*, and *r* is the radius of the roller. ω_i and v_{ir} are the angular speed and linear velocity of the roller in the frame *O-XY*, respectively. The transform matrix R_1 is defined as

$$R_1 = \begin{bmatrix} 0 & \sin\alpha_i \\ r & \cos\alpha_i \end{bmatrix}, \quad i = 1,2,3,4. \tag{10}$$

The generalized velocity of the roller's center, *o*, in the frame *O-XY* is determined by the coordinate transformation,

$$\begin{bmatrix} v_{ix} \\ v_{iy} \end{bmatrix} = \begin{bmatrix} \cos\theta_i & -\sin\theta_i \\ \sin\theta_i & \cos\theta_i \end{bmatrix}\begin{bmatrix} v'_{ix} \\ v'_{iy} \end{bmatrix} = R_2 R_1\begin{bmatrix} \omega_i \\ v_{ir} \end{bmatrix}, \quad i = 1,2,3,4, \tag{11}$$

where v_{ix} and v_{iy} are the velocities of the roller in the *X*- and *Y*-directions of the frame *O-XY*, respectively. θ_i is the attitude angle of the local frame *o-xy* in the frame *O-XY*. The coordinate transform matrix is

$$R_2 = \begin{bmatrix} \cos\theta_i & -\sin\theta_i \\ \sin\theta_i & \cos\theta_i \end{bmatrix}, \quad i = 1,2,3,4. \tag{12}$$

To attain the prescribed motion trajectory with the accompanying robot attitude angles, the inverse kinematics of the robot is utilized to calculate the necessary angular speeds of four ETCWs. The relationship between the generalized velocity of the roller's center v_{ix}, v_{iy}, and the generalized velocity of the robot in the frame *O-XY* is given by

$$\begin{bmatrix} v_{ix} \\ v_{iy} \end{bmatrix} = \begin{bmatrix} 1 & 0 & -L_{iY} \\ 0 & 1 & L_{iX} \end{bmatrix}\begin{bmatrix} v_x \\ v_y \\ \Omega \end{bmatrix} = R_3\begin{bmatrix} v_x \\ v_y \\ \Omega \end{bmatrix}, \quad i = 1,2,3,4, \tag{13}$$

where v_x and v_y are the velocities of the robot in the *X*- and *Y*-directions of the frame *O-XY*, respectively, and Ω is the angular speed of the robot. L_{iX} and L_{iY} are the *X*- and *Y*-directional components of the distance between the center of the roller and the center of the robot in the frame *O-XY*. The transform matrix R_3 is obtained by

$$R_3 = \begin{bmatrix} 1 & 0 & -L_{iY} \\ 0 & 1 & L_{iX} \end{bmatrix}. \tag{14}$$

By combining Eqs. (11) and (13), we obtain

$$R_2 R_1 \begin{bmatrix} \omega_i \\ v_{ir} \end{bmatrix} = R_3 \begin{bmatrix} v_x \\ v_y \\ \Omega \end{bmatrix}, \; i = 1, 2, 3, 4 \,. \tag{15}$$

The inverse kinematical equation of four roller speeds, ω_i, $i = 1,2,3,4$, for the given angular and linear velocities of the robot, Ω, v_x, v_y, is

$$\begin{bmatrix} \omega_1 \\ \omega_2 \\ \omega_3 \\ \omega_4 \end{bmatrix} = \frac{-\boldsymbol{R}}{r} \begin{bmatrix} v_x \\ v_y \\ \Omega \end{bmatrix}. \tag{16}$$

The Jacobian matrix $\boldsymbol{R}$ is defined by

$$\boldsymbol{R} = \begin{bmatrix} \dfrac{\cos(\theta_1 - \alpha_1)}{\sin\alpha_1} & \dfrac{\sin(\theta_1 - \alpha_1)}{\sin\alpha_1} & \dfrac{L_1 \sin(\theta_1 - \alpha_1 - \beta_1)}{\sin\alpha_1} \\ \dfrac{\cos(\theta_2 - \alpha_2)}{\sin\alpha_2} & \dfrac{\sin(\theta_2 - \alpha_2)}{\sin\alpha_2} & \dfrac{L_2 \sin(\theta_2 - \alpha_2 - \beta_2)}{\sin\alpha_2} \\ \dfrac{\cos(\theta_3 - \alpha_3)}{\sin\alpha_3} & \dfrac{\sin(\theta_3 - \alpha_3)}{\sin\alpha_3} & \dfrac{L_3 \sin(\theta_3 - \alpha_3 - \beta_3)}{\sin\alpha_3} \\ \dfrac{\cos(\theta_4 - \alpha_4)}{\sin\alpha_4} & \dfrac{\sin(\theta_4 - \alpha_4)}{\sin\alpha_4} & \dfrac{L_4 \sin(\theta_4 - \alpha_4 - \beta_4)}{\sin\alpha_4} \end{bmatrix}, \tag{17}$$

where $\beta_i = \arctan(L_{iX}/L_{iY})$, $i = 1,2,3,4$. $L_i = \sqrt{L_{iX}^2 + L_{iY}^2}$, $i = 1, 2, 3, 4$ are the distances between the four centers of the rollers to the center of the robot.

4.2   Installed angle of roller on ETCW

In general, the installed angle of the roller on the roller assembly shown in Fig. 5 is chosen as 30° to 50°.[33] For the convenience of analysis and control in this study, the roller's installed angle is set as $\alpha = 45°$, which is the angle between the axis normal to the roller's spindle and the local frame of the roller on the ETCW. In this arrangement, when the ETCW rotates and the rollers spin by themselves, the resultant force generated between the two rotations is along the direction of the roller spindle of 45°.[33] However, the omnidirectional movement of the ETCW is only

realized when the inverse kinematical Jacobian matrix **R** in Eq. (17) is full rank. In Fig. 18, several types of roller arrangement on the ETCW are shown.

The rank of each Jacobian matrix for the roller arrangements is listed in Table 2. From this table, it is shown that types 1, 2, and 4 can achieve omnidirectional movement because the corresponding Jacobian matrix is full rank. However, the type 4 arrangement is clearly not suitable for step-climbing of the robot. In the type 1 arrangement, the force in the direction of the axis spindle in contact with the ground is collinear with the center point of the robot. The robot struggles to rotate about the center point as a result, and controlling the motion trajectory becomes challenging. Therefore, in this study, the type 2 arrangement is used.

4.3   Case study of motion trajectory planning

The motion trajectory of the omnidirectional step-climbing robot is planned using a connected curve, which consists of a helix and a circle. In the coordinate system, the robot moves first from the starting point with coordinates (20, 0) and the attitude angle $\Theta = 0$ to the point with coordinates (−50, 0) and $\Theta = 1.5\pi$ along the helix within 20 s, $t \in [0, 20]$. Subsequently,
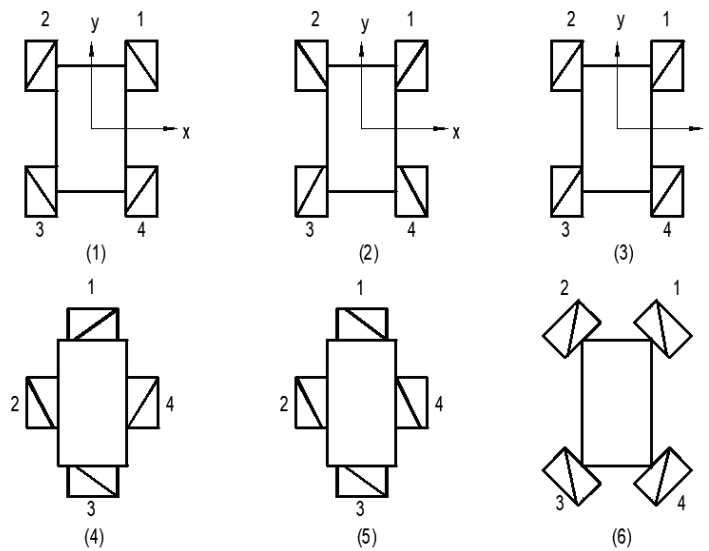

Fig. 18.   Typical roller arrangements.

Table 2
Rank of Jacobian matrix

No.	β_1	β_2	β_3	β_4	θ_1	θ_2	θ_3	θ_4	α_1	α_2	α_3	α_4	Rank
1	β_1	β_2	β_3	β_4	0	0	0	0	α	$-\alpha$	α	$-\alpha$	3
2	β_1	β_2	β_3	β_4	0	0	0	0	$-\alpha$	α	$-\alpha$	α	3
3	β_1	β_2	β_3	β_4	0	0	0	0	$-\alpha$	$-\alpha$	$-\alpha$	$-\alpha$	2
4	90°	180°	270°	0	90°	0	90°	0	α	α	$-\alpha$	$-\alpha$	3
5	90°	180°	270°	0	90°	0	90°	0	$-\alpha$	α	$-\alpha$	α	2
6	β_1	β_2	β_3	β_4	45°	−45°	45°	−45°	α	$-\alpha$	α	$-\alpha$	2

it completes one revolution around the circle in 20 s, $t \in (20, 40]$. Finally, the robot stops at the point $(-50, 0)$ and $\Theta = 1.5\pi$. The complete movement takes 40 s in total.

The prescribed trajectory is defined as

$$\text{Helix:} \begin{cases} X_1(\phi) = (20 + 30\phi/\pi)\cos(\phi) \text{ cm}, \\ Y_1(\phi) = (20 + 30\phi/\pi)\sin(\phi) \text{ cm}, \end{cases} 0 \le \phi \le \pi, t \in [0, 20], \tag{18}$$

$$\text{Circle:} \begin{cases} X_2(\phi) = 50\cos(\phi) \text{ cm}, \\ Y_2(\phi) = 50\sin(\phi) \text{ cm}, \end{cases} \pi \le \phi \le 3\pi, t \in (20, 40], \tag{19}$$

where the switching point between the two aforementioned curves is at $\phi = \pi$. The trajectory formed by the connected curve is shown in Fig. 19. Moreover, the attitude angle Θ of the front of the robot is also indicated by blue arrows at different locations.

To evaluate the required angular speeds of four ETCWs for achieving the predefined motion trajectory, it is also necessary to introduce the velocity information of the robot corresponding to the predefined trajectories. The first velocity functions for the robot moving along the helix in Eq. (18) are defined by

$$\begin{cases} v_{x1}(t) = \dot{\phi}_1 \left[30\cos(\phi_1)/\pi - (20 + 30\phi_1/\pi)\sin(\phi_1) \right] \text{ cm/s}, \\ v_{y1}(t) = \dot{\phi}_1 \left[30\sin(\phi_1)/\pi + (20 + 30\phi_1/\pi)\cos(\phi_1) \right] \text{cm/s}, \end{cases} t \in [0, 20]$$

$$\Omega_1(t) = \begin{cases} \dot{\phi}_1 t/10, & 0 \le t \le 10 \\ \dot{\phi}_1, & 10 < t \le 20 \end{cases} \text{rad/s} \tag{20}$$

where $\phi_1 = \dot{\phi}_1 t, t \in [0, 20]$, and $\dot{\phi}_1 = 0.075\pi$ rad/s.

The second velocity functions for the robot moving along the circle in Eq. (19) are given by
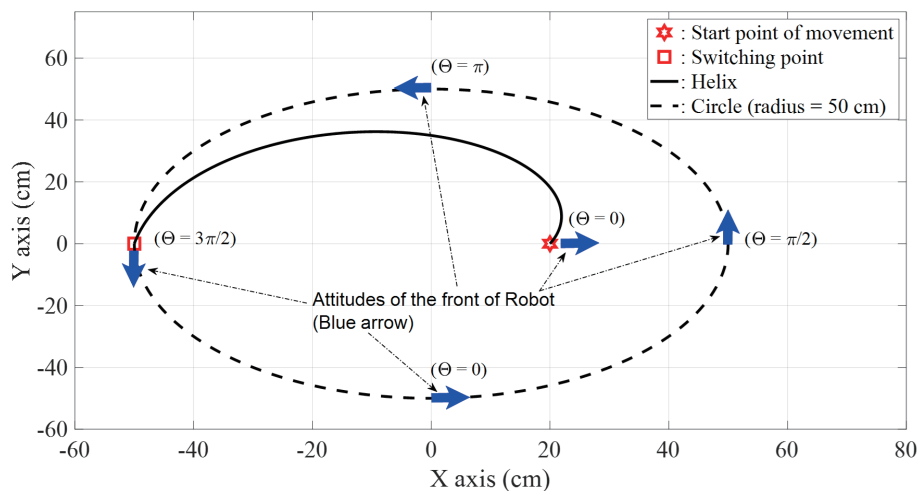

Fig. 19. (Color online) Planning motion trajectory of robot.

$$\begin{cases} v_{x2}(t) = -50\dot{\phi}_2 \sin(\phi_2)\ \text{cm/s}, \\ v_{y2}(t) = 50\dot{\phi}_2 \cos(\phi_2)\ \text{cm/s}, \end{cases} \phi_2 = \dot{\phi}_2(t-20) + 1.5\pi,\ t \in (20,\ 40]$$

$$\Omega_2(t) = \begin{cases} (\dot{\phi}_2 - \dot{\phi}_1)(t-20)/5 + \Omega_1(20), & 20 < t \le 25 \\ 0.1\pi, & 25 < t \le 40 \end{cases} \text{rad/s}$$

(21)

where $\dot{\phi}_2 = 0.1\pi$ rad/s. The time histories of the total velocity functions of the robot, including speeds in the X- and Y-directions, $V_x(t)$, $V_y(t)$, and the angular speed $\Omega(t)$, are shown in Fig. 20.

According to Eqs. (16) and (17) with the system parameters of the robot, $(L_{1X}, L_{1Y}) = (20, 15)$ cm, $(L_{2X}, L_{2Y}) = (21, 14)$ cm, and $(L_{iX}, L_{iY}) = (25, 18)$ cm, $i = 3,4$, the required angular speeds of the four ETCWs, $\omega_i(t)$, $i = 1,2,3,4$, for achieving the prescribed motion trajectory shown in Fig. 20 are evaluated. The results are shown in Fig. 21.
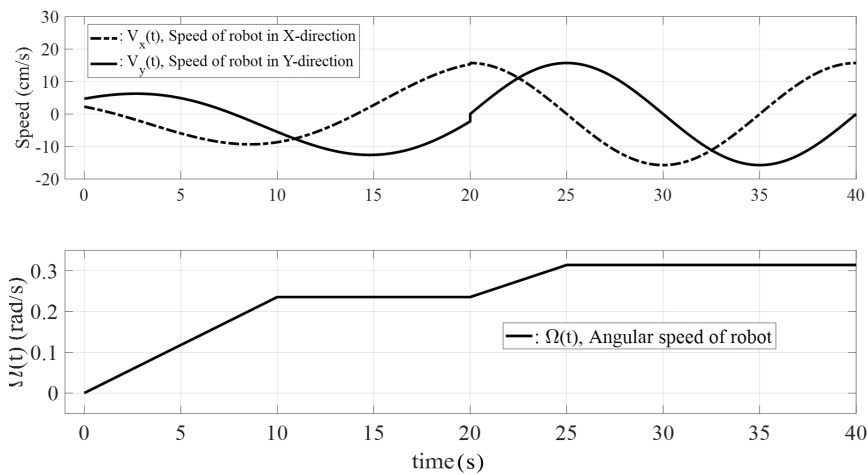

Fig. 20. (Color online) Time histories of the prescribed velocities of robot.
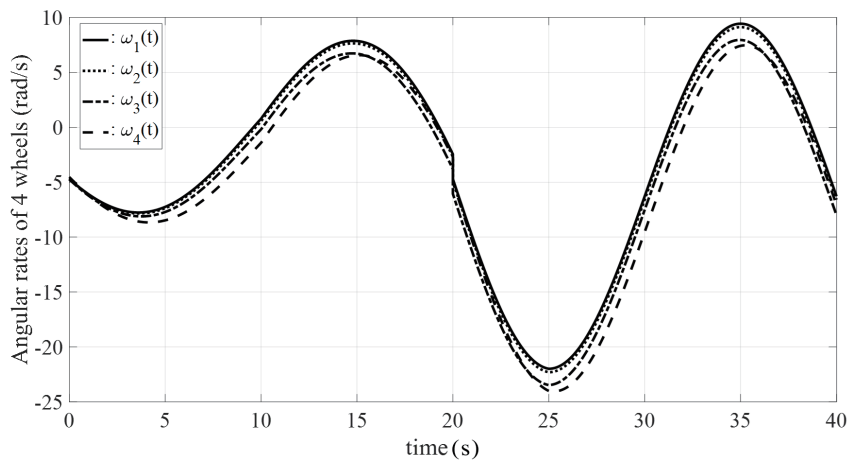

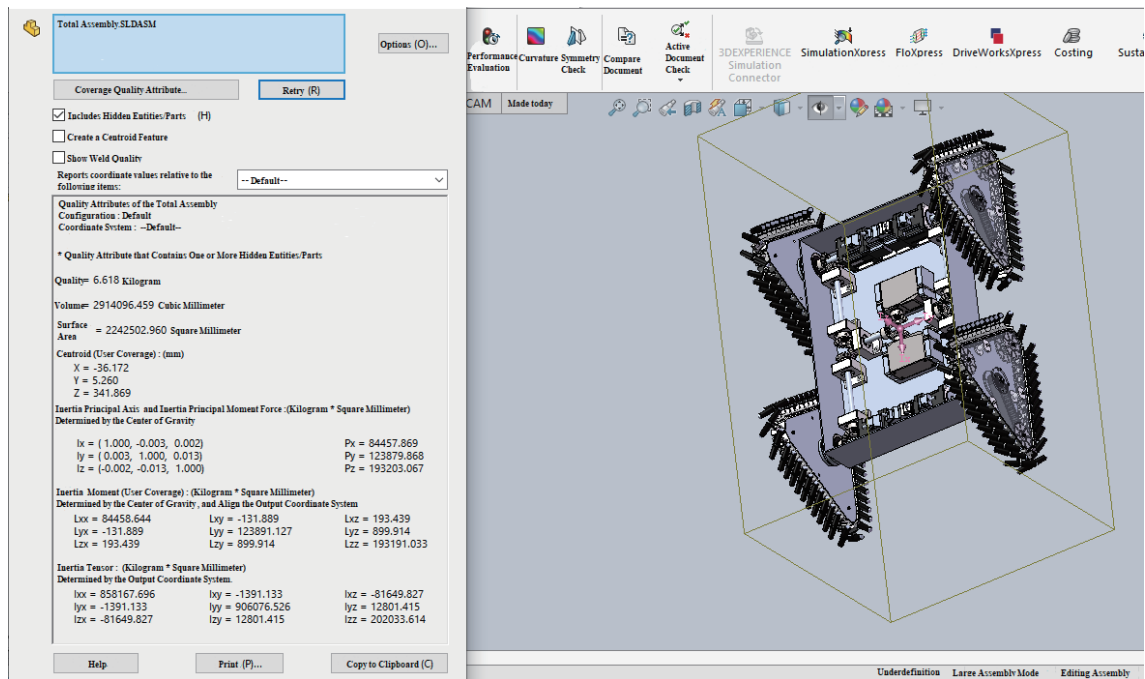Fig. 21. (Color online) Required angular speeds of four wheels.

Fig. 22.　(Color online) Overall assembly of robot.

5.　Overall Assembly of Omnidirectional Step-climbing Robot

The designed important modules of the robot, such as the ETCW, EAM, and supported modules, are completed. The overall assembly of the omnidirectional step-climbing robot is described finally using SOLIDWORKS software. As shown in Fig. 22, the mass of the robot is 6.618 kg, the volume is about 2914096.5 mm^3, and the surface area is about 2242503 mm^2.

6.　Conclusions

In the study, the design and analysis of a novel omnidirectional step-climbing robot are presented. The conclusions are as follows. (1) We introduced the innovative ETCW and built the structure design that allows a robot to move in any direction and climb steps without slipping. (2) To achieve smooth step-climbing, the EAM was also provided, which tunes the height of the base frame of the robot to avoid collision with the uneven ground during movement. (3) The designed models and the static analysis by the finite-element method of nonstandard supported parts, such as the chain link in the roller assembly, the L-type bearing seat, the base frame of the robot, the fixed frame of the RC servomotor, and the equilaterally triangular frame of the ETCW, were provided in detail. (4) The inverse kinematics of the robot were derived and the arrangements of the wheels and rollers are discussed. The case study of the motion trajectory was also carried out using MATLAB software. Finally, the overall assembly was performed using SOLIDWORKS software.

Acknowledgments

This work was supported in part by the Projects for the Department of Science and Technology of Fujian Province (Grant No. 2022-H-4009), the Science and Technology Projects of Sanming City (Grant No. 2022-G-16), the Operational Funding of the Advanced Talents for Scientific Research of Sanming University (Grant No. 19YG04), and the Teaching Reform Research Project of Sanming University (Grant Nos. J1910424 and J2010411).

References

1 J. Leng, H. Mou, J. Tang, Q. Li, and J. Zhang: Biomimetics **8** (2023) 183. https://doi.org/10.3390/biomimetics8020183
2 N. Ehrich Leonard: Springer Handbook of Ocean Engineering, M. R. Dhanak and N. I. Xiros Eds. (Springer, Cham, 2016). https://doi.org/10.1007/978-3-319-16649-0_19
3 B. Bayat, N. Crasta, A. Crespi, A. M. Pascoal, and A. Ijspeert: Curr. Opin. Biotechnol. **45** (2017) 76. https://doi.org/10.1016/j.copbio.2017.01.00
4 Q. Lu and Q. L. Han: IEEE Trans. Cybern. **49** (2019) 698. https://doi.org/10.1109/TCYB.2018.2879905
5 A. Farinelli, N. Boscolo, E. Zanotto, and E. Pagello: Rob. Auton. Syst. **90** (2017) 34. https://doi.org/10.1016/j.robot.2016.08.010
6 D. Wahrmann, A. C. Hildebrandt, C. Schuetz, R. Wittmann, and D. Rixen: J. Intell. Robot Syst. **93** (2019) 419. https://doi.org/10.1007/s10846-017-0746-8
7 N. Ahmed, S. Lee, and K. Nam: Sensors **23** (2023) 3184. https://doi.org/10.3390/s23063184
8 F. Weidinger, N. Boysen, and D. Briskorn: Transp. Sci. **52** (2018) 1297. https://doi.org/10.1287/trsc.2018.0826
9 H. Chen, Q. Wang, M. Yu, J. Cao, and J. Sun: Internet and Distributed Computing Systems (IDCS), Lecture Notes in Computer Science, vol 11226, Y. Xiang, J. Sun, G. Fortino, A. Guerrieri, J. Jung Eds. (Springer, Cham, 2018). https://doi.org/10.1007/978-3-030-02738-4_13
10 H. Li, J. Liu, C. Lyu, D. Liu, and Y. Liu: Electron. **12** (2023) 4693. https://doi.org/10.3390/electronics12224693
11 A. Ranjha, G. Kaddoum, and K. Dev: IEEE Trans. Ind. Inf. **18** (2022) 4954. https://doi.org/10.1109/TII.2021.3131608
12 Y. Li, C. Fu, H. Yang, H. Li, R. Zhang, Y. Zhang, and Z. Wang: Agric. **13** (2023) 1501. https://doi.org/10.3390/agriculture13081501
13 Z. Sun, S. Hu, H. Xie, H. Li, J. Zheng, and B. Chen: Comput. Electr. Eng. **105** (2023) 108529. https://doi.org/10.1016/j.compeleceng.2022.108529
14 K. Asadi, H. Ramshankar, H. Pullagurla, A. Bhandare, S. Shanbhag, P. Mehta, S. Kundu, K. Han, E. Lobaton, and T. Wu: Autom. Constr. **96** (2018) 470. https://doi.org/10.1016/j.autcon.2018.10.009
15 A. Y. Lee, H. C. Seo, and E. S. Park: Mach. **10** (2022) 1192. https://doi.org/10.3390/machines10121192
16 X. Zhao and C. C. Cheah: Autom. Constr. **146** (2023) 104647. https://doi.org/10.1016/j.autcon.2022.104647
17 Y. Ni, L. Li, J. Qiu, Y. Sun, G. Qin, Q. Han, and A. Ji: Biomimetics **7** (2022) 146. https://doi.org/10.3390/biomimetics7040146
18 F. Guo, S. Wang, D. Liu, and J. Wang: Chin. J. Mech. Eng. **36** (2023) 79. https://doi.org/10.1186/s10033-023-00897-3
19 J. Sun, Z. Sun, P. Wei, B. Liu, Y. Wang, T. Zhang, and C. Yan: Symmetry **15** (2023) 1091. https://doi.org/10.3390/sym15051091
20 J. Sun, Z. Sun, J. Li, C. Wang, X. Jing, Q. Wei, B. Liu, and C. Yan: Sensors **23** (2023) 4051. https://doi.org/10.3390/s23084051
21 W. Cai, Q. Li, S. Huang, H. Zhu, Y. Yang, and M. Zhao: IET Cyber-Syst. Robot **4** (2022) 298. https://doi.org/10.1049/csy2.12073
22 Y. Zhang, Y. Qian, Y. Ding, B. Hou, and R. Wang: Sci. Rep. **13** (2023) 19756. https://doi.org/10.1038/s41598-023-47022-x
23 L. Wang, R. Li, Z. Huangfu, Y. Feng, and Y. Chen: Actuators **12** (2023) 393. https://doi.org/10.3390/act12100393
24 Z. Wang, W. Wei, A. Xie, Y. Zhang, J. Wu, and Q. Zhu: Micromachines **13** (2022) 1688. https://doi.org/10.3390/mi13101688
25 D. Qin, G. Zhang, Z. Zhu, T. Chen, W. Zhu, X. Rong, A. Xie, and Y. Li: Int. J. Humanoid Rob. **2350013** (2023). https://doi.org/10.1142/S0219843623500135

26 A. A. Issa and A. A. Aldair: Iraqi J. Electr. Electron. Eng. **18** (2022) 117. https://doi.org/10.37917/ijeee.18.2.15

27 S. Aoi, T. Amano, S. Fujiki, K. Senda, and K. Tsuchiya: Front. Rob. AI **8** (2021) 697612. https://doi.org/10.3389/frobt.2021.697612

28 Z. Li, Y. Song, X. Zhang, X. Peng, and N. Xu: Appl. Sci. **13** (2023) 6876. https://doi.org/10.3390/app13126876

29 R. Morales, J. Chocoteco, V. Feliu, and H. Sira-Ramírez: Control Eng. Pract. **21** (2013) 604. https://doi.org/10.1016/j.conengprac.2013.01.006

30 K. Sasaki, Y. Eguchi, and K. Suzuki: Adv. Rob. **34** (2020) 802. https://doi.org/10.1080/01691864.2020.1757505

31 J. Lee, W. Jeong, J. Han, T. Kim, and S. Oh: Appl. Sci. **11** (2021) 5280. https://doi.org/10.3390/app11115280

32 N. J. Baishya, B. Bhattacharya, H. Ogai, and K. Tatsumi: Appl. Sci. **11** (2021) 7044. https://doi.org/10.3390/app11157044

33 A. Gfrerer: Comput. Aided Geom. Des. **25** (2008) 784. https://doi.org/10.1016/j.cagd.2008.07.008

34 B. I. Adamov: Russian J. Nonlinear Dyn. **14** (2018) 265. https://doi.org/10.20537/nd180209

35 B. I. Adamov and G. R. Saipulaev: Russian J. Nonlinear Dyn. **16** (2020) 291. https://doi.org/10.20537/nd200205

36 H. Taheri and C. X. Zhao: Mech. Mach. Theory **153** (2020) 103958. https://doi.org/10.1016/j.mechmachtheory.2020.103958

37 Y. Li, S. Ge, S. Dai, L. Zhao, X. Yan, Y. Zheng, and Y. Shi: Sensors **20** (2020) 75. https://doi.org/10.3390/s20010075

38 N. Adam, M. Aiman, W. M. Nafis, A. Irawan, M. Muaz, M. Hafiz, A. R. Razali, and S. N. S. Ali: MATEC Web of Conferences **90** (2017) 01077. https://doi.org/10.1051/matecconf/20179001077

39 N. Yamada, H. Komura, G. Endo, H. Nabae, and K. Suzumor: Proc. 2017 IEEE Int. Conf. Advanced Intelligent Mechatronics (AIM, 2017). https://doi.org/10.1109/AIM.2017.8014195

40 F. Hou, J. Yuan, K. Li, and Z. Wang: Int. J. Adv. Rob. Syst. March–April (2023) 1. https://doi.org/10.1177/17298806231163828

41 N. J. Baishya, B. Bhattacharya, H. Ogai, and K. Tatsumi: Actuators **10** (2021) 259. https://doi.org/10.3390/act10100259

42 M. Fieden and J. Bałchanowski: Appl. Sci. **11** (2021) 11778. https://doi.org/10.3390/app112411778

43 T. Takahashi, J. Zehnder, H. G. Okuno, S. Sugano, S. Coros, and B. Thomaszewski: IEEE Rob. Autom. Lett. **4** (2019) 4438. https://doi.org/10.1109/LRA.2019.2929984

44 H. Rothbart and T. Brown: Mechanical Design Handbook (McGraw-Hill, US, 2006) 2nd ed.